Application of the multiple sphere superposition solution to large–scale systems of spheres via an accelerated algorithm

D. W. Mackowski[a], L. Kolokolova[b]

[a]*Department of Mechanical Engineering, Auburn University, Auburn, AL 36849, U.S.A.*
[b]*Department Astronomy, University of Maryland, College Park MD 20742, U.S.A.*

Abstract

The application of an algorithm, based upon an FFT–enabled discrete Fourier convolution, to the multiple sphere superposition solution is presented. As opposed to the N_S^2 operation count scaling for the standard superposition solution algorithm, where N_S is the number of spheres, the accelerated algorithm results in closer to $N_S \ln N_S$ scaling. The new algorithm has been adopted into the Multiple Sphere T Matrix (MSTM) fortran-90 code, and the code has been optimized to allow for rapid calculation of configuration– and/or orientation–averaged radiative properties of large–scale systems of randomly–positioned spheres. Illustrative examples of the application of the updated code are presented.

1. Introduction

The purpose of this paper is to present recent extensions to the Multiple Sphere T Matrix (MSTM) code. MSTM is a fortran-90 implementation of the multiple sphere superposition solution to the frequency domain Maxwell's wave equations (MWEs). The original application of the code was focussed primarily on the calculation of extinction and absorption cross sections and scattering matrices for individual aggregates containing up to a few hundred monomer particles [1, 2]. With the development and increasing availability of large–scale multicore computational platforms, it has become possible – in terms of available memory resources – to apply the superposition solution to systems containing thousands of wavelength–sized monomers. The purposes of such calculations can be to predict scattering properties of macroscopically–large aggregates, and also to directly simulate the reflection and absorption properties of particulate media. [3, 4, 5, 6, 7, 8, 9, 10, 11]. In the latter case, it is necessary to apply the superposition solution to a sufficiently large target system of spheres – in both the number of spheres and the overall size of the target – so that the scattering and absorption produced by the target is representative of that produced by the modeled bulk medium. For example, a direct simulation of the reflectivity and absorptivity of a powder deposit could employ a cylindrically–shaped target, with an axial length corresponding to the deposit thickness

and a radius sufficiently larger than any other length scale present in the system, so that the target, as a whole, can approximate a plane–parallel medium.

Even with parallel platforms it is not difficult to reach a ceiling to the number of spheres, N_S, beyond which computations are either too expensive or too slow. The primary factor in this ceiling is the N_S^2 scaling of the computational effort necessary to calculate a solution. The exact solution is basically a linear many–body problem, and the state of any one sphere is coupled directly to the state of every other sphere. The coefficient matrix describing this coupling – which will scale as N_S – will be fully–populated, and performing a matrix–vector multiplication on this matrix, when done in the traditional, pair–of–nested–loops fashion, will involve N_S^2 operations.

The updated code employs an algorithm to significantly accelerate the solution process for large N_S. Originally identified by Chew et al.[12], the algorithm enables the calculation of the multiply–scattered field at each sphere via a discrete Fourier convolution process, and by using a Fast Fourier Transform (FFT) to accomplish this task the algorithm can approach $N_S \ln N_S$ operation count.

The paper will begin by briefly outlining the superposition solution formulation, followed by a more detailed description of the accelerated algorithm. The use of the code to calculate the reflectance and absorptance properties of layered particulate media, and the orientation–averaged polarimetric scattering properties of large–scale aggregates, are discussed and illustrative calculation examples are presented.

2. Formulation

2.1. Superposition solution background

To better focus on the salient aspects of the formulation, the presentation will be restricted to the case of homogeneous spheres comprised of optically inactive materials; the more general formulation used in the MSTM code allows for spheres–within–spheres and optically active sphere material [13]. In what follows all lengths are made dimensionless by scaling with the free space wavenumber $k_0 = 2\pi/\lambda_0$. The target system consists of N_S spheres, each specified by a (dimensionless) radius a^i, complex refractive index m^i, and a position vector $\mathbf{r}^i = (X^i, Y^i, Z^i)$ relative to a common target origin.

The superposition solution takes the complex electric field amplitude at points external to the spheres to be the sum of the incident and the scattered fields,

$$\mathbf{E}(\mathbf{r}) = \mathbf{E}_{inc}(\mathbf{r}) + \sum_{i=1}^{N_S} \mathbf{E}_{sca,i}(\mathbf{r}), \quad \mathbf{r} \in V_{ext} \tag{1}$$

The individual fields are mathematically approximated by truncated vector spherical wave function (VSWF) expansions, given by

$$\mathbf{E}_{inc}(\mathbf{r}) = \sum_{\mathbf{n}}^{M^0} f_{\mathbf{n}}^0 \mathbf{N}_{\mathbf{n}}^{(1)}(\mathbf{r} - \mathbf{r}^0) \tag{2}$$

$$\mathbf{E}_{sca,i}(\mathbf{r}) = \sum_{\mathbf{n}}^{M_S^i} a_{\mathbf{n}}^i \mathbf{N}_{\mathbf{n}}^{(3)}(\mathbf{r} - \mathbf{r}^i) \tag{3}$$

In the above, $\mathbf{N}_\mathbf{n}^{(t)}$ is the VSWF of type $t = 1$ (regular) and 3 (outgoing). The single bold subscript $\mathbf{n}$ is a 3-vector $\mathbf{n} = (n_1, n_2, n_3)$, for VSWF degree $n_1 = 1, 2, \ldots L_S^i$, azimuth order $n_2 = -n_1 : n_1$, and mode $n_3 = 1, 2$ (for TE, TM), and L_S^i denotes the truncation degree of the expansion for sphere i which typically scales with dimensionless radius a^i per the Mie criteria. The vector index summation notation implies a three–fold summation over VSWF degree, order, and mode. For a given sphere i, the set of scattering coefficients, $a_\mathbf{n}^i$, will have $M_S^i = 2L_S^i(L_S^i + 2)$ members.

The scattering coefficients are unknowns and are sought from the solution. On the other hand, the expansion coefficients for the incident field relative to the target origin, denoted as $f_\mathbf{n}^0$, will depend on the polarization state, propagation direction (specified by the polar and azimuth angles β, α in a spherical coordinate system centered on the target origin), and the general form (plane wave, Gaussian beam) of the incident field; whatever the case, it is assumed that the $f_\mathbf{n}^0$ are known quantities. The set of incident field coefficients contains $M^0 = 2L^0(L^0 + 2)$ members, and the degree truncation L_0 used in Eq. (2) would be that needed for the expansion to describe, to a set precision, the incident field on the surface of each sphere in the target system. This truncation will typically scale with R_C, where R_C is the dimensionless circumscribing radius of the target.

The solution is obtained by a merging of the addition theorem for VSWF with Mie theory. At points on the surface of sphere i the external field can be approximated by a pair of VSWF expansions centered about the origin of i. One part of the pair will be an outgoing expansion corresponding to the scattered field from i, and the other will be a regular expansion corresponding to the exciting field at i. This latter part will appear as

$$E_{exc,i}(\mathbf{r})|_{|\mathbf{r}-\mathbf{r}^i|=a^i} = \sum_{\mathbf{n}=1}^{M_S^i} (g_\mathbf{n}^i + f_\mathbf{n}^i)\, \mathbf{N}_\mathbf{n}^{(1)}(\mathbf{r} - \mathbf{r}^i) \tag{4}$$

with f and g describing the direct and secondary parts to the exciting field,

$$f_\mathbf{n}^i = \sum_\mathbf{l}^{M_0} J_{\mathbf{n}\mathbf{l}}(\mathbf{r}^i - \mathbf{r}^0)\, f_\mathbf{l}^0 \tag{5}$$

$$g_\mathbf{n}^i = \sum_{\substack{j=1 \\ j \neq i}}^{N_S} \sum_\mathbf{l}^{M_S^i} H_{\mathbf{n}\mathbf{l}}(\mathbf{r}^i - \mathbf{r}^j)\, a_\mathbf{l}^j \tag{6}$$

where $H(\mathbf{r}^2 - \mathbf{r}^1)$ and $J(\mathbf{r}^2 - \mathbf{r}^1)$ are matrices which transform either an outgoing or a regular VSWF expansion centered about origin 1 into a regular VSWF expansion centered about 2; they are functions solely of the translation vector between the origins and the refractive index of the background medium. Equations (4) and (6) are subject to the restriction that $a^i < |\mathbf{r}^i - \mathbf{r}^j|$, and this condition will always be met when the spheres are located external to each other. Equation (5) holds for any incident field that is created by sources located outside R_C. For the specific case of plane wave incidence Eq. (5) can be replaced with a simple phase–shift relation.

Mie theory provides the relationship between the scattered and exciting fields at sphere i, in the form

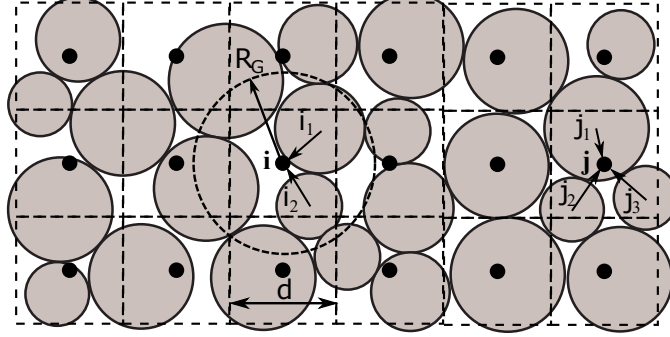$$a_\mathbf{n}^i = \bar{a}_\mathbf{n}^i\, (g_\mathbf{n}^i + f_\mathbf{n}^i) \tag{7}$$

3

Figure 1: Sphere and node configuration

where the Mie coefficient for i, denoted as $\bar{a}_{\mathbf{n}}^i$, depends on the dimensionless sphere radius and refractive index. The condensed order/degree/mode index $\mathbf{n}$ will be retained when referring to $\bar{a}_{\mathbf{n}}^i$, yet it is noted that this quantity is independent of azimuthal order.

Combining the previous results in a system of linear equations for the scattering coefficients:

$$a_{\mathbf{n}}^i - \bar{a}_{\mathbf{n}}^i \sum_{\substack{j=1 \\ j \neq i}}^{N_S} \sum_{\mathbf{l}}^{M_S^i} H_{\mathbf{n}\mathbf{l}}(\mathbf{r}^i - \mathbf{r}^j)\, a_{\mathbf{l}}^j = \bar{a}_{\mathbf{n}}^i\, f_{\mathbf{n}}^i \qquad (8)$$

For identical spheres with equal truncation orders $L_S^i = L_S$, Eq. (8) forms $N_{eqns} = 2L_S(L_S + 2)N_S$ complex–valued equations for the set of scattering coefficients. Equation (8) represents the implicit solution to the multiple sphere superposition problem. Determination of the polarimetric scattering properties of the target, for a set incident direction, requires solution of Eq. (8) for two mutually orthogonal incident linear polarizations. Such solutions are most efficiently obtained using iteration methods.

2.2. Secondary field via the discrete Fourier convolution

An iteration solution to Eq. (8), when performed using standard matrix–vector multiplication algorithms, will have an operation count that scales with N_S^2. Even on multiple core, parallel computational platforms, it is not difficult to reach a ceiling to N_S beyond which the standard iterative solution to Eq. (8) is either too expensive or too slow. A method for substantially reducing the scaling was introduced by Chew et al. [12], and can be viewed as a hybrid between the FFT–accelerated convolution process employed in discrete dipole models [14], and the fast multipole method (FMM) [11]. Basically, the method uses the first stage of a FMM to transform the outgoing fields from the individual, arbitrarily–positioned spheres into a regular lattice of outgoing fields. The regular lattice structure then enables the application of the discrete Fourier convolution to calculate the interactions among points on the lattice. The lattice fields are then re-transformed into the sphere–centered fields. The key feature of this algorithm is that the computational effort is reduced, under optimal conditions, to $N_S \ln(N_S)$ scaling.

Consider the target configuration depicted in Fig. (1). A regular grid having a specified spacing d is mapped onto the target volume. The grid forms a lattice of control

volumes, each with volume d^3, and the central point within the control volume will be referred to as a node. Denote a node position index by the convention $\mathbf{i} = (n_x\hat{\mathbf{x}}, \, n_y\hat{\mathbf{y}}, \, n_z\hat{\mathbf{z}})$ with $n_x, \, n_y, \, n_z$ representing integers. The spheres in the target can now be divided into node sets, denoted as $N(\mathbf{i})$, so that $N(\mathbf{i})$ includes all spheres $i_1, i_2, \ldots i_{N(\mathbf{i})}$ whose origin lies within the control volume associated with $\mathbf{i}$, as illustrated in Fig. (1).

Referring to Fig. (1), the exciting field at sphere i_1, due to the outgoing field at j_1, can approximated as

$$\sum_{\mathbf{l}}^{M_S} H_{\mathbf{n}\mathbf{l}}(\mathbf{r}^{i_1} - \mathbf{r}^{j_1})a_{\mathbf{l}}^{j_1} \approx \sum_{\mathbf{n}'}^{M_G} J_{\mathbf{n}\mathbf{n}'}(\mathbf{r}^{i_1} - \mathbf{r}^{\mathbf{i}}) \sum_{\mathbf{l}'}^{M_G} H_{\mathbf{n}'\mathbf{l}'}(\mathbf{r}^{\mathbf{i}} - \mathbf{r}^{\mathbf{j}}) \sum_{\mathbf{l}}^{M_S} J_{\mathbf{l}'\mathbf{l}}(\mathbf{r}^{\mathbf{j}} - \mathbf{r}^{j_1})a_{\mathbf{l}}^{j_1} \quad (9)$$

This approximation is valid providing the distance between the nodes $\mathbf{i}, \mathbf{j}$ exceeds that between the spheres i_1, j_1 and their associated nodes. This will always be met when the circumscribing spheres associated with cells $\mathbf{i}, \mathbf{j}$ are non–overlapping, and for a cubic grid (scalar d) this implies $|\mathbf{i} - \mathbf{j}| \geq \sqrt{3}$. The formula appears as an approximation solely because it is assumed that the summations over $\mathbf{n}'$ and $\mathbf{l}'$ are truncated at the finite grid degree L_G, with $M_G = 2L_G(L_G + 2)$. Along with the grid spacing d, the grid degree L_G will be a parameter in the algorithm, and their effect on the accuracy and efficiency of the algorithm will be discussed further on.

Define the node–based scattering and exciting field coefficients by

$$a_{\mathbf{n}}^{\mathbf{i}} = \sum_{i \in N(\mathbf{i})} \sum_{\mathbf{l}}^{M_S} J_{\mathbf{n}\mathbf{l}}(\mathbf{r}^{\mathbf{i}} - \mathbf{r}^{i}) \, a_{\mathbf{l}}^{i} \quad (10)$$

$$g_{\mathbf{n}}^{\mathbf{i}} = \sum_{|\mathbf{j}-\mathbf{i}|\geq r_h} \sum_{\mathbf{l}}^{M_G} H_{\mathbf{n}'\mathbf{l}}(d(\mathbf{i} - \mathbf{j})) \, a_{\mathbf{l}}^{\mathbf{j}} \quad (11)$$

in which r_h denotes the exclusion (or 'hole') radius associated with the grid, which again is $\sqrt{3}$ for a cubic grid. The exciting field at sphere i can now be formulated as a neighboring sphere part and a grid part:

$$g_{\mathbf{n}}^{i} = \sum_{\substack{j \in N^+(\mathbf{i}) \\ j \neq i}} \sum_{\mathbf{l}}^{M_S} H_{\mathbf{n}\mathbf{l}}(\mathbf{r}^{i} - \mathbf{r}^{j}) \, a_{\mathbf{l}}^{j} + \sum_{\mathbf{l}}^{M_G} J_{\mathbf{n}\mathbf{l}}(\mathbf{r}^{i} - \mathbf{r}^{\mathbf{i}}) \, g_{\mathbf{l}}^{\mathbf{i}} \quad (12)$$

The set $N^+(\mathbf{i})$, in the sum over j, denotes the set of neighbor spheres associated with node $\mathbf{i}$ and corresponds to all spheres in the sets $N(\mathbf{i}')$ for which $|\mathbf{i}' - \mathbf{i}| < r_h$. The exciting field coefficients in Eq. (11) can be computed using a DFC, as the summation over position involves only lattice sites.

The key parameters in the algorithm are the grid spacing d and the grid degree truncation L_G. For a fixed system of spheres the total number of nodes will scale as $N_G \sim 1/d^3$, and application of a simple Mie–type truncation criterion would suggest that $L_G \sim d$. The DFC part of the algorithm has a computational effort which scales as $L_G^2 N_G \ln N_G \sim 1/d \ln d$, resulting in lower computational effort for increasing d. On the other hand, a bigger d/smaller N_G will result in a higher computational effort for the nearest–neighbor and sphere–to–node parts of the algorithm, and as N_G shrinks to

5

unity, the algorithm obviously reverts to the standard, sphere–to–sphere direct route. A series of computational tests indicate that the optimum performance of the algorithm is achieved when $N_G \approx N_S$. For this case – and for sphere systems in the shape of a rectangular solid – each node has, on average, one associated sphere. This minimizes the number of 'wasted' nodes with no associated spheres, yet also minimizes the average translation distance between the spheres and their associated nodes. This behavior is incorporated into the code to enable an automatic selection of d and L_G.

The accelerated algorithm does put greater demands on computer memory than the standard algorithm. Considering the zero–padding requirements of the discrete Fourier convolution algorithm, the Fourier–transformed node-to-node translation matrix in Eq. (11) will occupy $2^3 \times M_G \times N_G$ memory locations. This number could be significantly smaller than the $N^2_{eqns} = M^2_S N^2_S$ memory locations required to store the sphere–to–sphere translation matrices in Eq. (8), yet storage of the matrices is not required to iteratively solve Eq. (8) via the standard route, nor does such storage significantly decrease the solution time as on–the–fly calculation of H^{i-j} can be performed relatively fast [15]. On the other hand, the accelerated algorithm does require complete memory storage of the node–to–node translation matrix.

The DFC algorithm was implemented into the MSTM fortran–90 code [1]. The DFT was performed using the generalized 2,3,5–prime factor FFT algorithm of Temperton [16], which is used in the current DDSCAT discrete dipole approximation code [17].

2.3. Cross sections, scattering matrix, and other calculated target properties

For a given incident polarization state $p = 1, 2$, the scattered electric field complex amplitude, at points outside the circumscribing sphere, can be described by a single outgoing VSWF expansion centered on the target origin $\mathbf{r}^0$ and truncated at L^0, via

$$\mathbf{E}_{sca,p}(\mathbf{r}) = \sum_{\mathbf{n}}^{M^0} a^0_{\mathbf{n},p} \, \mathbf{N}^{(3)}_{\mathbf{n}}(\mathbf{r} - \mathbf{r}^0) \tag{13}$$

with expansion coefficients given by

$$a^0_{\mathbf{n},p} = \sum_{i=1}^{N_S} \sum_{\mathbf{l}}^{M^i_S} J_{\mathbf{n}\mathbf{l}}(\mathbf{r}^0 - \mathbf{r}^i) \, a^i_{\mathbf{l},p} \tag{14}$$

The scattered field in Eq. (13) is defined with respect to the target coordinate system, for which scattering angle $\theta = 0$ corresponds to the $+z$ axis direction; this coordinate frame is appropriate for simulations of reflection from particulate layers. On the other hand, simulations of scattering from large aggregates will use the conventional particle scattering scheme, i.e., $\theta = 0$ corresponding to the incident direction. This can be accomplished by performing a rotation operation, through the incident directions β, α, on the target–origin scattering coefficients [18].

The dimensionless extinction and scattering cross sections of the target (using area

scale of $1/k_0^2$) for unpolarized incidence are given by

$$C_{ext} = -\pi \sum_{p=1}^{2} \sum_{\mathbf{n}}^{M^0} \text{Re} \left[a_{\mathbf{n},p}^0 f_{\mathbf{n},p}^{0*} \right] \tag{15}$$

$$C_{sca} = \pi \sum_{p=1}^{2} \sum_{\mathbf{n}}^{M^0} \left| a_{\mathbf{n},p}^0 \right|^2 \tag{16}$$

The absorption cross section of an individual sphere is given by [19]

$$C_{abs}^i = -\pi \sum_{p=1}^{2} \sum_{\mathbf{n}}^{M_S^i} \text{Re} \left(\frac{1}{\bar{a}_{\mathbf{n}}^i} + 1 \right) \left| a_{\mathbf{n},p}^i \right|^2 \tag{17}$$

and by energy conservation,

$$\sum_{i=1}^{N_S} C_{abs}^i = C_{ext} - C_{sca} \tag{18}$$

The 2×2 amplitude matrix for the target, evaluated at a given scattering direction θ, ϕ, is obtained from the far–field limit of Eq. (13); the VSWFs for this case are replaced by the vector spherical harmonic functions. The 4×4 scattering matrix $S_{ij}(\theta, \phi)$, $i, j = 1 : 4$ is obtained from conjugated products of the amplitude matrix elements, and can be expressed analytically in θ, ϕ as an expansion, to truncation degree $2L^0$, of generalized spherical functions [18, 20]. In particular, the $S_{11}(\theta, \phi)$ element can be expressed as a spherical harmonic expansion, i.e.,

$$S_{11}(\theta, \phi) = \sum_{n=0}^{2L^0} \sum_{m=-n}^{n} c_{mn} P_n^m(\cos \theta) e^{im\phi} \tag{19}$$

with $c_{00} = C_{sca}/4\pi$ to satisfy the scattered energy balance.

The cross sections and scattering matrix defined above are implicitly a function of the orientation of the target with respect to the incident direction. When the target is simulating an aggregated particle – as opposed to a particle layer – the orientation–averaged scattering properties of the target are typically sought. Such properties can be obtained analytically from the T matrix of the target, and the T matrix can be obtained from M^0 solutions to Eq. (8), using $f_1^0 = \delta_{\mathbf{l}'-1}$ for all $\mathbf{l}'$ in M^0 [18]. We have used this feature in previous investigations to examine EM scattering by randomly–oriented aggregated particles containing a moderate (i.e., 100's) of spheres [4, 21, 22].

More recently, we have come to the conclusion that random–orientation properties of large–scale aggregates can be more efficiently calculated by a hybrid analytical+numerical scheme that does not involve T matrix calculation. The scattering matrix of a randomly–oriented particle must be a function of θ only, and as a consequence only the azimuth–independent parts of the scattering matrix expansion (i.e., $m = 0$ in Eq. (19)) will contribute to the orientation–averaged expansion. For aggregates that are roughly spherical and uniform, these $\phi-$invariant parts of S, along with the absorption and scattering cross sections, will be relatively insensitive to β, α. As a result, the number of quadrature points in β and α needed to obtain an accurate average will be significantly less than

the number of solutions M^0 needed to calculate the full T matrix, and this discrepancy increases as R_C (and, correspondingly, M^0) increases. The code retains the analytical, T–matrix based algorithm for computing orientation–averaged properties, and this option may be better for aggregates with scattering properties that are highly dependent on incident direction.

The reflection and absorption by an H thick, plane–parallel particle layer can be approximated by that from a finite volume target, of cylindrical or rectangular geometry with thickness H and radius or half–width R_T. The directional–hemispherical reflectance of the layer is obtained from the integral of S_{11} over the incidence–facing hemisphere, divided by the lateral area of the target. This calculation can be done analytically using the expansion in Eq. (19). Numerical experiments have found that the directional absorptance is most accurately calculated by omitting absorption by spheres near the lateral edges of the target. Specifically, a cylindrical sample volume centered within the target, of radius $R_{samp} \sim 0.75 R_T$ and thickness H is specified. The directional absorptivity is then calculated from the sum of the sphere absorption cross sections within the sample volume, divided by πR_{samp}^2.

The required lateral dimension R_T of the target is simply that which, upon further increase, results in insignificant change in the calculated layer properties of the target. It can be anticipated, and results bear out, that $R_T \gg H$ for this limit to occur, and as a consequence this simulation method can quickly become numerically impractical for large H. One way around this problem is to model the infinite–width, H thick layer as a 2D periodic system, of periodic width W, for which the target volume becomes a $W \times W \times H$ unit cell. This approach has been used in discrete dipole and related volume–discretized formulations, which are applicable to monomer particles of arbitrary shape[23, 24]. A multipole–based, multiple sphere formulation of the 2D periodic layer reflection model has been recently presented in [25]. The 2D periodic approach, however, introduces its own set of complications, such as oscillations and singularities associated with periodic lattice modes and the diffraction–pattern nature of the scattered field.

An alternative, hybrid approach to calculating reflection properties of dense and thick particulate layers is to use direct simulation methods to calculate the properties of a relatively thin layer, and then use the layer properties in a plane–parallel RT algorithm (such as the adding–doubling method) to calculate the properties of arbitrarily–thick layers. In this regard, the layer thickness H need only be sufficiently large to capture the correlation statistics among the spheres. We are working on this approach now, and will present the results in a forthcoming publication.

3. Results and Discussion

3.1. Accelerated interaction algorithm performance

An indication of the performance benefit offered by the fast interaction algorithm is presented in Fig. (2). The plot shows the CPU time for solution of the sphere interaction equations as a function of the number of spheres in the target, using the traditional and convolution–based algorithms for computing the exciting field at each sphere. The spheres have unit dimensionless radius and a refractive index of $\mathsf{m} = 1.6 + 0.0123\mathsf{i}$, and the sphere–based VSWF expansions were truncated at $L_S = 3$. The code was run on a HP Z820 workstation in parallel mode using 4 cores. The squares correspond to
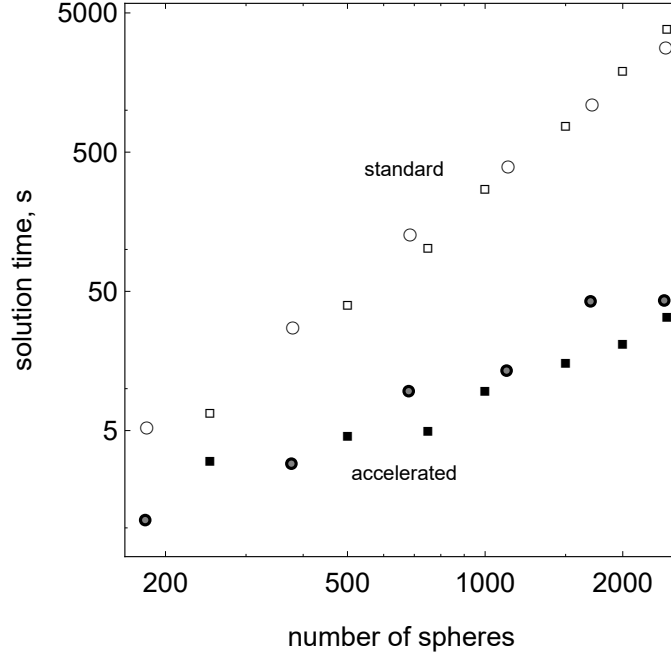
Figure 2: Solution time vs. N_S, for standard and FFT-accelerated algorithms. Squares: constant volume cubic target. Circles: constant volume fraction spherical target.

spheres randomly distributed within a cube of width $W = 15$, so that sphere volume fraction increases with N_S, whereas the circles have the spheres randomly distributed in a variable–radius spherical target, with volume fraction fixed at $f_V = 0.25$. For each solution the number of nodes is set to as close as possible to the number of spheres – while maintaining the FFT requirements on the grid dimensions – and the node spacing is adjusted accordingly. The node truncation order was set using the simple criteria

$$L_G = \max\left(\text{ceiling}\,(d+1),\; L_S\right) \qquad (20)$$

and this resulted in cross sections calculated using standard and accelerated algorithms agreeing to around 1-2 percent.

The results in Fig. (2) clearly demonstrate the efficacy of the accelerated algorithm. A simple power–law fit of the results show that the solution time for the standard algorithm follows close to a N_S^3 scaling, whereas that for the accelerated algorithm goes as $N_S^{1.4}$; the higher–than–expected proportionality is due to the number of iterations required for a solution increasing with N_S. For the specific conditions, the accelerated algorithm leads to over a 100–fold increase in solution time when N_S is in excess of 10^3. The results for a cubic target show the best improvement of the accelerated algorithm; this is expected as the rectangular grid can fit entirely within the target with no wasted nodes, whereas only around $\pi/6$ of the nodes will be within the spherical target.
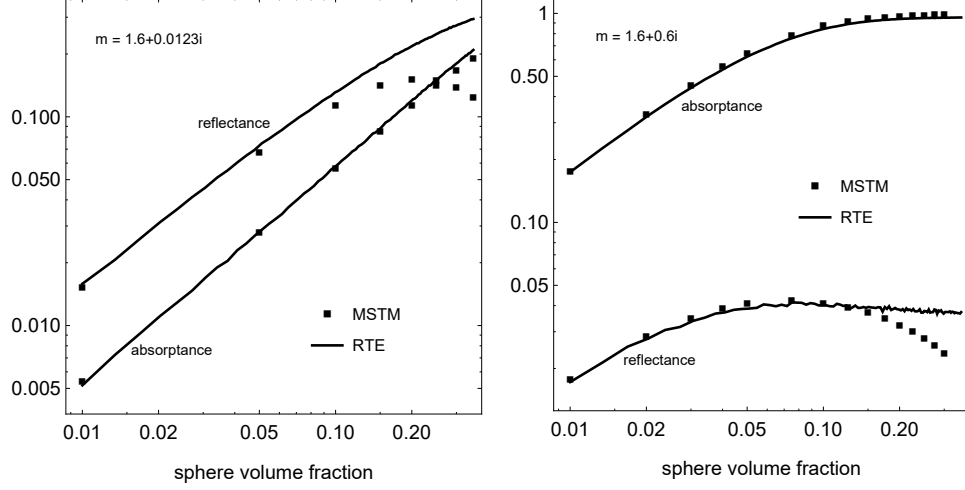
9

Figure 3: Directional–hemispherical reflectance, and directional absorptance, of a constant–thickness layer as a function of sphere volume fraction, as calculated by MSTM and monte carlo RT. Sphere radius $a = 1$, layer thickness $H = 20$.

3.2. Simulation of layer properties

Examples of layer simulation calculation results are presented in Fig. (3). Shown in the plots are the directional–hemispherical diffuse reflectance and directional absorptance of a spherical particle layer as a function of the sphere volume fraction. The spheres have unit radius and a refractive index of $m = 1.6 + 0.0123i$ (left) and $m = 1.6 + 0.6i$ (right), and incidence is normal. The target geometry used in the MSTM simulations was rectangular with a lateral width of 60 and a thickness of 20. Configurations were generated by randomly sampling sphere positions within the target volume and rejecting positions which overlap with previously–positioned spheres. The smallest (0.01) and largest (0.35) volume fractions corresponded to $N_S = 171$ and 6016.

Each MSTM point in Fig. (3) corresponds to the average of 100 randomly–sampled configurations; the variation in the MSTM–calculated reflectance, from configuration to configuration, was around 2 to 10 percent on a relative basis, with lower N_S resulting in larger variations. The code is designed to optimize the configuration–averaging process on multi–core platforms. Specifically, each solution, for a given configuration, is assigned to a group of 4 cores; this number represents an optimum for the biconjugate–gradient iteration method (requiring 2 matrix-vector multiplications per iteration), along with the fact that 2 solutions are needed per configuration (the 2 incident polarization states). A configuration–average job running on P cores is distributed so that $P/4$ configurations are done in parallel. As each solution is basically independent of others – communication is needed only at the end of the solution to update the averaged quantities – the parallel scaling of the process is basically ideal. The computations in Fig. (3) were performed on an HP Z820 using 20 cores, and each point represents the average of 100 configurations. For the $N_S = 6016$ case, a solution for a single configuration took around 20 min, yet the entire set of 100 configurations took around 20 min$\times 100/(20/4) = 400$ min. Machines

10

with larger numbers of cores would run the job proportionally faster.

Shown also in Fig. (3) are reflectance and absorptance as predicted by the RTE for the target geometry and sphere properties. A simple monte carlo RT code, designed solely to predict hemispherical reflectance and absorptance, was used for this purpose. The extinction coefficient, albedo, and scattering phase function of the medium, used to sample path lengths, absorption fractions, and scattering trajectories of computational photons, were predicted using Lorenz/Mie theory.

The results in Fig. (3) clearly show the transition from and independent to dependent scattering regime as sphere volume fraction increases beyond five to ten percent. For the specific particle properties used here, this effect is seen solely in the reflection properties of the layer. An increasing sphere volume fraction results in a decrease in the apparent sphere scattering cross section, and this effect is sufficiently strong so that, for volume fractions exceeding 0.1-0.2, the reflectance decreases with increasing particle volume in the layer. The MSTM–predicted absorptance of the layer, on the other hand, closely follows RT behavior throughout the range of volume fraction. Our observations suggest that this behavior holds for order–wavelength sized spheres of the type used in Fig. (3). It cannot be assumed that the same behavior will extend to metallic or highly refractive particles.

3.3. Application to large fractal particles

The test case examined in the previous section –that being a densely-packed target in the form of a rectangular solid – would likely be the situation which maximizes the speed improvement over the standard algorithm. However, the accelerated algorithm significantly shortens computations for spheres randomly positioned into a spherical volume or for fractally–built aggregates. This capability of the code is in high demand within the astronomical community, as the results of the Rosetta mission to comet 67P/Churyumov-Gerasimenko showed that dust agglomerates with sizes on the order of hundreds of μm [26] dominate the dust size distributions at distances 100 km from the nucleus. It was also shown in [27] that that model computations of opposition and negative polarization effects, observed at small phase angles (large scattering angles) for asteroids and satellites, approach the observed values with increasing the number of particles in the model volume and radius of the volume.

In Figs. (4)-(6) we present computation results for BPCA (Ballistic Particle Cluster Aggregates) particles having porosity ($= 1$-f_V) of 88 percent [28]. The use of this aggregate model allows us to compare our current computations with results obtained with the original MSTM code [31, 32]. The BPCA particle model has proved its validity to model the results of photopolarimetric observations of comets [33, 34]. The computations were performed at the NASA HECC cluster Pleiades (Haswell nodes), using 960 processors of speed 2.5 GHz each, for more details see [35]. Resource constraints on this platform imposed an upper limit of $N_S \sim 2 \times 10^4$ for unit–radius monomers; for visible wavelengths and the BPCA model this maximum N_S corresponds an aggregate circumscribing radius of ~ 10 μm. The maximum N_S is also a factor of 10 greater than that feasible with the original MSTM code.

The effect on aggregate brightness and polarization on the number of monomers is shown in Fig. (4). Monomers have unit radius, and refractive indices of ice ($\mathsf{m} = 1.31$) and Halley dust ($\mathsf{m} = 1.98 + 0.48\mathsf{i}$), the latter a mixture of silicates, organics, carbon, and iron representative the composition of the dust in comet Halley [29, 30]. As shown
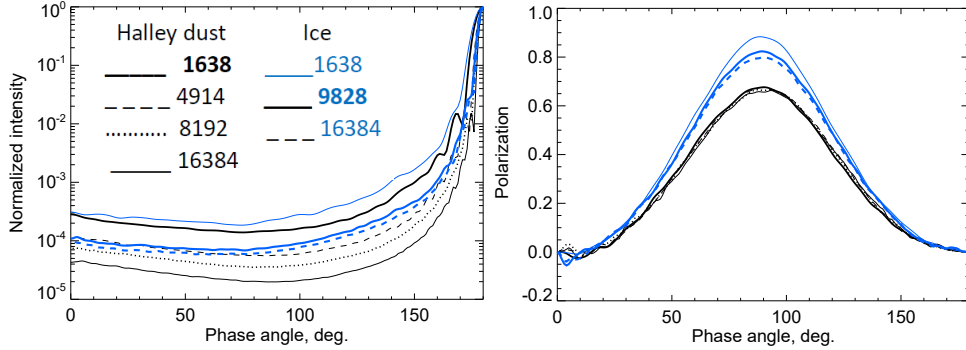
11

Figure 4: Modeled dependence on normalized brightness and polarization on the properties of aggregates of different number of monomers for icy (blue) and Halley dust (see [33]) particles. The monomers of radius 0.1 μm and aggregates of porosity 85% are modeled.
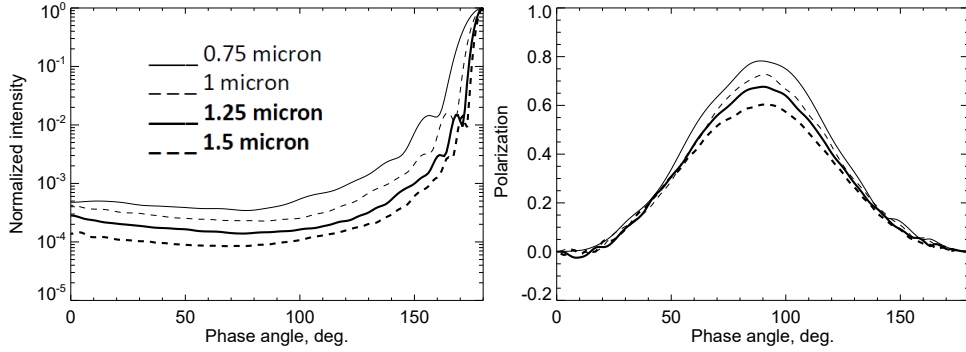

Figure 5: Modeled dependence on normalized brightness and polarization on the size of monomers. $N_S = 1638$, porosity 85%.

in Fig. (4), N_S affects the maximum of polarization. However, with increasing N_S, the maximum appears to approach a saturation value. The value of N_S at which this saturation occurs depends on the monomer refractive index, and it is evident that this saturation stabilizes faster for more absorbing materials. This is an interesting result that provides a hope that to model cometary particles we do not need to model aggregates of overall size approaching 100s of μm.

Additional modeling was performed to check the effects of monomer size. Our results confirmed previous results for smaller aggregates [27] that photopolarimetric properties of aggregates strongly depend on the monomer size. This strongly affects the polarization as well as the brightness phase curve even if a very narrow range of sizes is analyzed. The results are shown in Fig. (5), and correspond to Halley dust and a wavelength of 0.65 μm.

The most intriguing results we have obtained explore the effect of the particle material, i.e., of the complex refractive index. Results are presented in Fig. (6), which show brightness and polarization as a function of phase angle for BPCA particles. Monomers
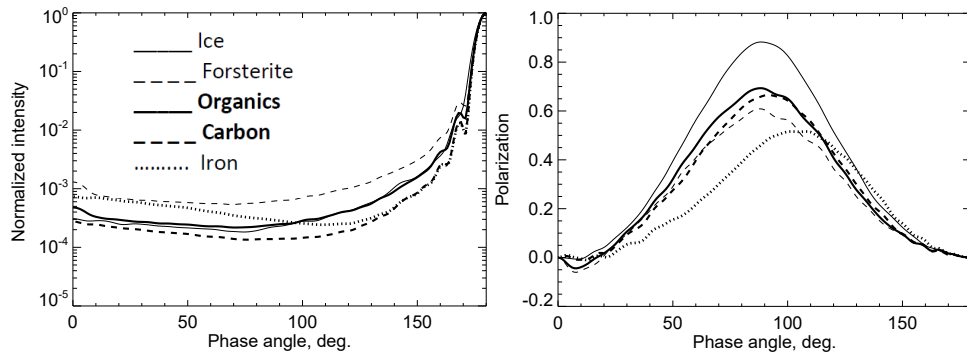
Figure 6: Modeled dependence on normalized brightness and polarization for aggregates made of different materials. Monomers radius 0.1 μm, N_S =1638, porosity 85%.

have unit radius, and refractive indices of the listed materials are given in [36]. It is clear from Fig. (6) that the phase curves of brightness and polarization do not show a straightforward, easily–identified dependence on real or imaginary part of the refractive index. Considerably more computational experiments, involving variations in monomer and aggregate size would be needed to sort out the effect of monomer refractive index from that on monomer size, number of monomers, and aggregate porosity.

4. Summary

We believe that the accelerated solution algorithm, combined with parallel processing architectures, allow the MSTM code to directly simulate the EM scattering and absorption characteristics of particle layers and macroscopically–large particle aggregates. The computations performed here suggest that, for particles with order–wavelength radii, a radiative transport model can provide an acceptable estimate of particle layer reflectance and absorptance for particle volume fractions up to 10 percent. We also demonstrate that the accelerated algorithm, combined with large–scale parallel processing platforms, make feasible the computational modeling of realistically–sized comet dust particles.

The updated MSTM code used to perform the test calculations can be downloaded from [37].

Acknowledgements

References

[1] D. W. Mackowski, M. I. Mishchenko, A multiple sphere T-matrix Fortran code for use on parallel computer clusters, "J. Quant. Spectrosc. Radiat. Transfer" 112 (2011) 2182–2192.

[2] D. Mackowski, L. Kolokolova, W. Sparks, T-matrix approach to calculating circular polarization of aggregates made of optically active materials, "J. Quant. Spectrosc. Radiat. Transfer" 112 (11) (2011) 1726–1732.

13

[3] M. I. Mishchenko, L. Liu, D. W. Mackowski, B. Cairns, G. Videen, Multiple scattering by random particulate media: exact 3D results., Opt. Express 15 (6) (2007) 2822–36.
URL http://www.ncbi.nlm.nih.gov/pubmed/19550586

[4] D. W. Mackowski, M. I. Mishchenko, Direct simulation of multiple scattering by discrete random media illuminated by Gaussian beams, Phys. Rev. A 83 (1) (2011) 013804–+. doi:10.1103/PhysRevA.83.013804.

[5] V. P. Tishkovets, E. V. Petrova, M. I. Mishchenko, Scattering of electromagnetic waves by ensembles of particles and discrete random media, J. Quant. Spectrosc. Radiat. Transfer 112 (13) (2011) 2095 – 2127. doi:http://dx.doi.org/10.1016/j.jqsrt.2011.04.010.
URL http://www.sciencedirect.com/science/article/pii/S0022407311001683

[6] K. Muinonen, M. I. Mishchenko, J. M. Dlugach, E. Zubko, A. Penttilä, G. Videen, Coherent backscattering verified numerically for a finite volume of spherical particles, The Astrophysical Journal 760 (2) (2012) 118.
URL http://stacks.iop.org/0004-637X/760/i=2/a=118

[7] D. Mackowski, M. Mishchenko, Direct simulation of extinction in a slab of spherical particles, ”J. Quant. Spectrosc. Radiat. Transfer” 123 (2013) 103 – 112.
URL http://www.sciencedirect.com/science/article/pii/S0022407313000629

[8] A. Penttilä, Quasi-specular reflection from particulate media, J. Quant. Spectrosc. Radiative Transfer(2013).

[9] A. Egel, L. Pattelli, G. Mazzamuto, D. S. Wiersma, U. Lemmer, Celes: Cuda-accelerated simulation of electromagnetic scattering by large ensembles of spheres, Journal of Quantitative Spectroscopy and Radiative Transfer 199 (2017) 103–110. doi:https://doi.org/10.1016/j.jqsrt.2017.05.010.
URL https://www.sciencedirect.com/science/article/pii/S0022407317301772

[10] L. Ma, J. Tan, J. Zhao, F. Wang, C. Wang, Multiple and dependent scattering by densely packed discrete spheres: Comparison of radiative transfer and maxwell theory, Journal of Quantitative Spectroscopy and Radiative Transfer 187 (2017) 255–266. doi:https://doi.org/10.1016/j.jqsrt.2016.09.025.
URL https://www.sciencedirect.com/science/article/pii/S0022407316304137

[11] J. Markkanen, A. J. Yuffa, Fast superposition t-matrix solution for clusters with arbitrarily-shaped constituent particles, Journal of Quantitative Spectroscopy and Radiative Transfer 189 (2017) 181–188. doi:https://doi.org/10.1016/j.jqsrt.2016.11.004.
URL https://www.sciencedirect.com/science/article/pii/S0022407316306550

[12] W. C. Chew, J. H. Lin, X. G. Yang, An fft t-matrix method for 3d microwave scattering solutions from random discrete scatterers, Microwave and Optical Technology Letters 9 (4) (1995) 194–196. arXiv:https://onlinelibrary.wiley.com/doi/pdf/10.1002/mop.4650090408, doi:https://doi.org/10.1002/mop.4650090408.
URL https://onlinelibrary.wiley.com/doi/abs/10.1002/mop.4650090408

[13] D. Mackowski, A general superposition solution for electromagnetic scattering by multiple spherical domains of optically active media, ”J. Quant. Spectrosc. Radiat. Transfer” 133 (2014) 264 – 270.

[14] J. Goodman, B. T. Draine, P. J. Flatau, Application of fast-fourier-transform techniques to the discrete-dipole approximation, Opt. Lett 16 (15) (1991) 1198–1200.

[15] D. W. Mackowski, Analysis of radiative scattering for multiple sphere configurations, Proc. Roy. Soc. Lond. A 433 (1991) 599–614.

[16] C. Temperton, Implementation of a self-sorting in-place prime factor fft algorithm, J. Computational Physics 58 (3) (1985) 283–299.

[17] B. Draine, P. Flatau, User guide for the discrete dipole approximation code ddscat 7.3, arXiv preprint arXiv:1305.6497 (2013).

[18] D. W. Mackowski, M. I. Mishchenko, Calculation of the T matrix and the scattering matrix for ensembles of spheres, J. Opt. Soc. Amer. A 13 (1996) 2266–2278.

[19] D. W. Mackowski, Calculation of total cross sections of multiple sphere clusters, J. Opt. Soc. Amer. A 11 (1994) 2851–2861.

[20] J. W. Hovenier, C. V. van der Mee, H. Domke, Transfer of polarized light in planetary atmospheres: basic concepts and practical methods, Vol. 318, Springer Science & Business Media, 2014.

[21] M. Mishchenko, L. Liu, D. W. Mackowski, B. Cairns, G. Videen, Multiple scattering by random particulate media: exact 3D results, Opt. Express 15 (2007) 2822–2836.

[22] M. I. Mishchenko, D. W. Mackowski, Coherent backscattering in the cross-polarized channel, Phys. Rev. A 83 (1) (2011) 013829. doi:10.1103/PhysRevA.83.013829.

[23] B. Draine, P. Flatau, Discrete-dipole approximation for periodic targets: theory and tests, JOSA A 25 (11) (2008) 2693–2703.

[24] D. W. Mackowski, B. Ramezanpour, A plane wave model for direct simulation of reflection and transmission by discretely inhomogeneous plane parallel media, J. Quant. Spectrosc. Radiat. Transfer 213 (2018) 95–106.

[25] D. Theobald, D. Beutel, L. Borgmann, H. Mescher, G. Gomard, C. Rockstuhl, U. Lemmer, Simulation of light scattering in large, disordered nanostructures using a periodic t-matrix method, J. Quant. Spectrosc. Radiat. Transfer 272 (2021) 107802. doi:https://doi.org/10.1016/j.jqsrt.2021.107802.
URL https://www.sciencedirect.com/science/article/pii/S0022407321002958

[26] C. Güttler, T. Mannel, A. Rotundi, S. Merouane, M. Fulle, D. Bockelée-Morvan, J. Lasue, A. Levasseur-Regourd, J. Blum, G. Naletto, H. Sierks, Synthesis of the morphological description of cometary dust at comet 67p/churyumov-gerasimenko, Astronomy & Astrophysics 630 (2019) A24.

[27] R. A. West, Optical properties of aggregate particles whose outer diameter is comparable to the wavelength, Applied optics 30 (36) (1991) 5316–5324.

[28] H. Kimura, L. Kolokolova, A. Li, J. Lebreton, Light scattering and thermal emission by primitive dust particles in planetary systems, in: Light Scattering Reviews, Volume 11, Springer, 2016, pp. 363–418.

[29] I. Mann, H. Kimura, L. Kolokolova, A comprehensive model to describe light scattering properties of cometary dust, Journal of Quantitative Spectroscopy and Radiative Transfer 89 (1-4) (2004) 291–301.

[30] E. Jessberger, A. Christoforidis, J. Kissel, Aspects of the major element composition of halley's dust, Nature 332 (1988) 691–695.

[31] L. Kolokolova, D. Mackowski, Polarization of light scattered by large aggregates, Journal of Quantitative Spectroscopy and Radiative Transfer 113 (18) (2012) 2567–2572.

[32] L. Kolokolova, L. Nagdimunov, D. Mackowski, Light scattering by hierarchical aggregates, Journal of Quantitative Spectroscopy and Radiative Transfer 204 (2018) 138–143.

[33] H. Kimura, L. Kolokolova, I. Mann, Optical properties of cometary dust. Constraints from numerical studies on light scattering by aggregate particles, Astron. Astrophys. 407 (2003) L5–L8. doi:10.1051/0004-6361:20030967.

[34] H. Kimura, L. Kolokolova, I. Mann, Light scattering by cometary dust numerically simulated with aggregate particles consisting of identical spheres, Astron. Astrophys. 449 (2006) 1243–1254.

[35] www.nas.nasa.gov/hecc/resources/pleiades.html.

[36] O. Ivanova, I. Lukyanyk, L. Kolokolova, H. S. Das, M. Husárik, V. Rosenbush, V. Afanasiev, J. Svoreň, N. Kiselev, V. Krushinsky, Photometry, spectroscopy, and polarimetry of distant comet c/2014 a4 (sonear), Astronomy & Astrophysics 626 (2019) A26.

[37] Multiple–sphere codes are available at www.eng.auburn.edu/users/dmckwski/scatcodes.

15